
Convolutional Generation of Textured 3D Meshes

Dario Pavlo

Dept. of Computer Science
ETH Zurich

Graham Spinks

Dept. of Computer Science
KU Leuven

Thomas Hofmann

Dept. of Computer Science
ETH Zurich

Marie-Francine Moens

Dept. of Computer Science
KU Leuven

Aurelien Lucchi

Dept. of Computer Science
ETH Zurich

Abstract

Recent generative models for 2D images achieve impressive visual results, but clearly lack the ability to perform 3D reasoning. This heavily restricts the degree of control over generated objects as well as the possible applications of such models. In this work, we leverage recent advances in differentiable rendering to design a framework that can generate *triangle meshes* and associated high-resolution texture maps, using only 2D supervision from single-view natural images. A key contribution of our work is the encoding of the mesh and texture as 2D representations, which are semantically aligned and can be easily modeled by a 2D convolutional GAN. We demonstrate the efficacy of our method on Pascal3D+ Cars and the CUB birds dataset, both in an unconditional setting and in settings where the model is conditioned on class labels, attributes, and text. Finally, we propose an evaluation methodology that assesses the mesh and texture quality separately.

1 Introduction

State-of-the-art image generative models based on the GAN framework [10] nowadays achieve photorealistic results thanks to a series of key contributions in this area including [16, 31, 32, 59, 22]. A recent trend in this field has been to make generative models more controllable and of better use for downstream applications. This includes works that condition generative models on class labels [32, 59, 3], text [60, 61, 53, 27], input images [64, 19], as well as structured scene layouts such as semantic maps [47, 36, 33], bounding boxes [63, 17, 41], and scene graphs [20]. While these approaches achieve impressive visual results, they are all based on architectures that fundamentally ignore the concept of image formation. Real-world images depict 2D projections of 3D objects, and explicitly considering this aspect would lead to better generative models that can provide disentangled control over shape, color, pose, lighting, and can better handle spatial phenomena such as occlusions. A recent trend to account for such effects has been to disentangle factors of variation during the generation process in the hope of making it more interpretable [57, 38, 22, 23]. These approaches potentially learn a hierarchical decomposition of objects and in some settings (e.g. faces) they can provide a limited degree of control over pose. However, the pose disentanglement assumptions made by these approaches have been shown to be unrealistic without some form of supervision [29], and they have not reached the degree of controllability that a native 3D representation would be capable of.

In this work, we propose a GAN framework for generating *triangle meshes* and associated textures, using only 2D supervision from single-view natural images. In terms of applications, our approach could greatly facilitate content creation for art, movies, video games, virtual reality, as well as augment the possible downstream applications of generative models. We leverage recent advances in differentiable rendering [30, 24, 28, 4] to incorporate 3D reasoning into our approach. In particular, we initially adopt a reconstruction framework to estimate meshes through a representation we name *convolutional mesh* which consists of a displacement map that deforms a mesh template in its tangent space. This representation is particularly well-suited for 2D convolutional architectures as both the mesh and its texture share the same topology, and the mesh benefits from the spatial smoothness property of convolutions. We then project natural images onto the UV map (mapping between

texture coordinates and mesh vertices) and reduce the problem to a 2D modeling task where the representation is independent of the pose of the object. Finally, we train a 2D convolutional GAN in UV space where inputs to the discriminator are masked in order to deal with occlusions.

Our model generates realistic meshes and can easily scale to high-resolution textures (512×512 and possibly more) owing to the precise semantic alignment between maps in UV space, without requiring progressive growing [22]. Most importantly, since our model is based exclusively on 2D convolutions, we can easily adapt ideas from state-of-the-art GAN methods for 2D images, and showcase our approach under a wide range of settings: conditional generation from class labels, attributes, text (with and without attention), as well as unconditional generation. We evaluate our approach on Pascal3D+ Cars [51] and CUB Birds [46], and propose metrics for evaluating FID scores [16] on meshes and textures separately as well as collectively. In summary, we make the following contributions:

- A novel convolutional mesh representation that is smooth by definition, and alongside the texture, is easy to model using standard 2D convolutional GAN architectures.
- A GAN framework for producing textured 3D meshes from a pose-independent 2D representation. In a GAN setting, we are the first to demonstrate full generation of textured triangle meshes using 2D supervision from *natural images*, whereas prior attempts have focused on very limited settings supervised on synthetic data without a principled texture learning strategy.
- We demonstrate *conditional* generation of 3D meshes from text (with and without an attention mechanism) and show that our model provides disentangled control over shape and appearance.
- We will soon release our code and data, including class and attribute annotations that we collected for Pascal3D+.

2 Related work

Deep learning approaches that deal with 3D data typically target either *reconstruction*, where the goal is to predict a 3D mesh from an image, or *generation*, where the goal is to produce meshes from scratch. We review the literature of both tasks as they are relevant to our work.

3D representations. Early approaches have focused on reconstructing meshes using 3D supervision. These are typically based on voxel grids [9, 5, 66, 49, 55, 42, 12], point clouds [7], or signed distance functions [35]. However, 3D supervision requires ground-truth 3D meshes, which are typically available in synthetic datasets but not for real-world images. Therefore, a related line of research aims at reconstructing meshes using exclusively 2D supervision from images. Similarly, there has been work on voxel representations [54, 11, 44, 48, 43, 56] as well as on point clouds [18], but these methods require supervision from multiple views which still limits their applicability. More recent approaches lift the requirement of multiple views in order to learn to reconstruct 3D shapes from a single view using a voxel representation [15]. However, these representations tend to be computationally inefficient and do not explicitly support texture maps.

Differentiable rendering. Triangle meshes are an established representation in computer graphics, owing to their efficiency as well as flexibility in terms of vertex transformations and texturing. For this reason, they are used in almost every graphics pipeline, ranging from video games to animation. This has motivated a newer line of research where the goal is to predict triangle meshes and texture maps from single images, achieving high-quality visual results [24, 21, 4]. The basic building block of these approaches is a *differentiable renderer* (DR), i.e. a renderer that can compute gradients w.r.t. the scene parameters. While early DRs approximate gradients with respect to mesh vertices [30, 24], newer methods propose fully-differentiable formulations [28, 4]. Our work is also based on this framework, and specifically we adopt DIB-R [4] because it supports UV mapping.

3D mesh generation. Analogous to reconstruction methods, 3D object generation has also been demonstrated using voxels [50, 9, 39, 52, 65, 2] and point clouds [1, 8], but again, these approaches require some form of 3D supervision which precludes training from natural images, in addition to the texturing limitations highlighted above. As for triangle meshes, [4] propose a GAN framework where 2D images are discriminated after differentiable rendering, but they rely on multiple views of synthetic objects and cannot directly learn textures from images. Instead, they supervise the generator on textures predicted by a separate model previously trained for reconstruction. This intermediate step results in a noticeable loss of quality, and is absent in our approach, which can learn from natural images directly. A parallel work to ours [14] also leverages 2D data to generate 3D meshes, but they adopt a VAE framework [26] and only predict face colors instead of UV-mapped textures (i.e. *texture*

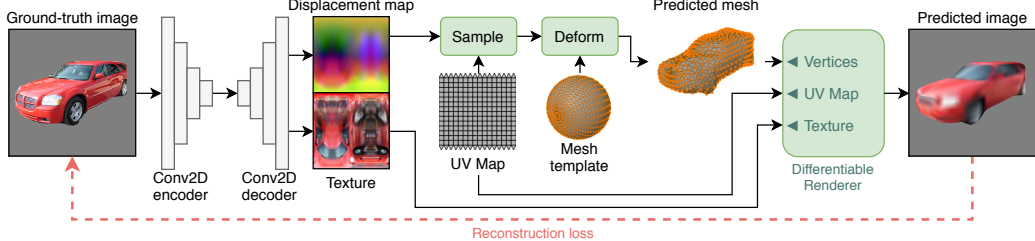


Figure 1: Initial mesh reconstruction using our convolutional mesh representation. This step follows a typical autoencoder setup where the goal is to reconstruct the input image after forcing it through a 3D representation and rendering it. RGB colors in the displacement map correspond to XYZ coordinates.

maps), which limits the visual detail of generated objects. An early work [37] generates untextured meshes in a variational framework using reinforcement learning to estimate gradients. Our work is based on GANs and can explicitly generate high-resolution texture maps which are then mapped to the mesh via UV mapping, enabling an arbitrary level of detail. Unlike [4], we learn textures directly from natural images, and introduce a pose-independent representation that reduces the problem to a 2D modeling task. Finally, we are not aware of any prior work that can generate 3D meshes from text.

3 Method

Requirements. Our approach has data requirements similar to recent *reconstruction* methods [21, 4]. We require a dataset of single-view natural images, with annotated segmentation masks and pose, or alternatively, keypoints from which the pose can approximately be estimated. If ground-truth masks are not available (as in the ImageNet subset of Pascal3D+), we obtain them from an off-the-shelf segmentation model (we use Mask R-CNN [13]), whereas the pose is inferred from the keypoints using structure-from-motion, as was done in [21]. Our approach does not require ground-truth 3D meshes (i.e. 3D supervision) or multiple views of the same object.

Mesh representation. As mentioned, we focus on triangle meshes due to their wide adoption in computer graphics, their flexibility in terms of vertex transformations, and their support for texture mapping. Following [24, 21, 4], we use a deformable sphere template with a fixed topology and a static UV map which maps vertices to texture coordinates. Previous work has used fully-connected networks to predict vertex positions, which ignores the topology of the mesh and the spatial correlation between neighboring vertices, essentially treating each vertex as independent. This issue is typically mitigated through regularization, e.g. by combining smoothness [24] and Laplacian [40] loss penalties. Instead, we propose to regress the mesh through the same deconvolutional network that we use to regress the texture. The output is therefore a *displacement map* (Fig. 1), which describes how the mesh should be deformed in its tangent space. The displacement map and the texture share the same UV map, which ensures that the maps are topologically aligned (e.g. the vertices corresponding to the beak of a bird are co-located with the color of the beak). This detail is crucial for designing a discriminator that can jointly discriminate mesh and texture, that is, not just the mesh and texture separately, but also how well the texture fits the mesh. Furthermore, our mesh representation is smooth by nature since it benefits from the intrinsic spatial correlation of convolutional layers. A second major difference in terms of representation is that our mesh template is a *UV sphere* (2-pole sphere as shown in Fig. 1), whereas prior work has used ico-spheres. While the latter exhibits a more regular mesh, it cannot be UV-mapped without gaps or arbitrary distortions that make the representation space discontinuous. On the other hand, except for the singularities at the two poles, a UV sphere presents a bijective mapping between vertices and texture coordinates, has a well-defined tangent map, and the circular boundary conditions along the x axis can be neatly incorporated in the model architecture using circular convolutions. Denoting the mesh template as \mathbf{V} (an $N \times 3$ matrix with N vertices described by their xyz coordinates, where each vertex is indexed by i), the final position of the i -th vertex is computed as $\mathbf{v}_i + \mathbf{R}_i \Delta_{\mathbf{v}_i}$ where $\Delta_{\mathbf{v}_i}$ is the output of the model after sampling the displacement map, and \mathbf{R}_i is a precomputed rotation matrix that describes the local normal, tangent, and bitangent of the vertex.

3.1 Pose-independent dataset

Our approach initially consists in augmenting the dataset with mesh estimates (Fig. 1) and converting 2D images into a pose-independent representation (Fig. 2), finally modeled by a 2D GAN (Fig. 3).

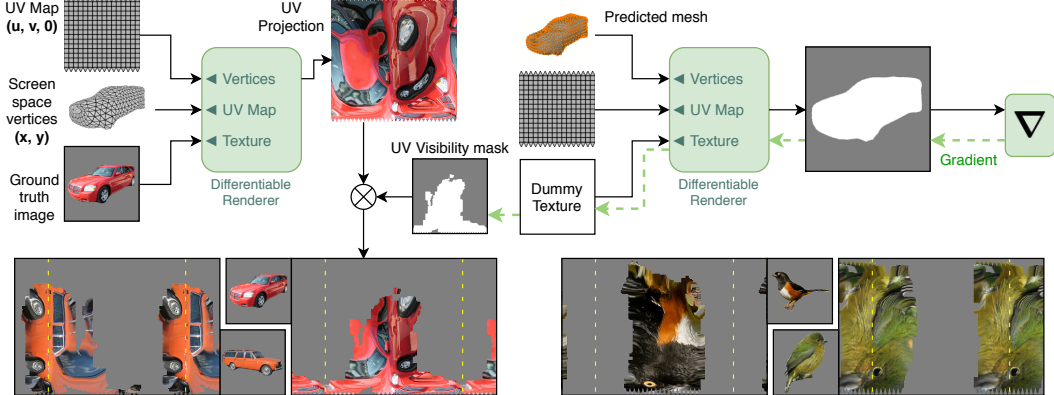


Figure 2: Projection of ground-truth images onto the UV map, producing *pseudo-ground-truth* textures. The bottom row shows additional examples (Pascal3D+ Cars on the left and CUB Birds on the right). The yellow dashed lines represent the boundaries of the textures, which have been extended to highlight the circular boundary conditions along the x axis.

Mesh estimation. This is a typical reconstruction task where the goal is to reconstruct the mesh from an input image. Our approach is loosely based on [21], but simplified since we are not interested in performing inference on unseen images. Our formulation can be regarded as a fitting process where we only keep the predicted meshes and discard the model/textures. As depicted in Fig. 1, the input image is fed to a convolutional encoder, compressed into a vector representation, and decoded through a convolutional decoder which jointly outputs a texture and a displacement map. The predicted texture is only used to facilitate the learning process and produce more semantically-aligned meshes, and is discarded afterwards. The mesh template is deformed as described by the displacement map, and the final result is rendered using a differentiable renderer. The model is trained to minimize the mean squared error (MSE) between the rendered image and the input image. While this generally leads to blurry textures, it does not represent an issue in our case as these textures are discarded. Since we are not interested in performing inference, we do not predict pose or keypoints, nor do we use texture flows or perceptual losses to improve predicted textures. For the camera model, we adopt a weak-perspective model where the pose of an image is described by a rotation $\mathbf{q} \in \mathbb{R}^4$ (a unit quaternion), a scale $s \in \mathbb{R}$, and a screen-space translation $\mathbf{t} \in \mathbb{R}^2$. For Pascal3D+, we augment the projection model with a perspective correction term \mathbf{z}_0 (further details in the Appendix A.2). While these are initially estimated using structure-from-motion on keypoints [21], we allow the optimizer to fine-tune s , \mathbf{t} , and \mathbf{z}_0 (if used), i.e. we additionally optimize with respect to the dataset parameters¹. This leads to a better alignment between rendered masks and ground-truth masks, facilitating the next step.

2D discrimination. The most obvious way to adapt the aforementioned reconstruction framework is to train a GAN where the generator \mathbf{G} produces a 3D mesh and the discriminator \mathbf{D} discriminates its 2D projection after differentiable rendering, as in [4]. However, we found this strategy to lead to training instabilities due to the discrepancies of the representation being used by \mathbf{G} and \mathbf{D} (which are respectively pose-independent and pose-dependent). A further complication we observed is an aliasing effect in the gradient from the differentiable renderer. Successful 2D GAN models typically use complementary architectures for \mathbf{G} and \mathbf{D} (e.g. both convolutional), which motivates our next idea.

Pose-independent representation. We instead propose to project ground-truth images onto the UV map of the mesh template, thus reducing the generative model to a 2D GAN that can be trained with existing convolutional techniques. The construction of this representation is depicted in Fig. 2, and can be regarded as a form of *inverse rendering*. We treat our previous mesh estimates as if they were texture coordinates, i.e. $(x, y) \rightarrow (u, v)$ (z is dropped), the UV map becomes the mesh to render (a flat surface with $z = 0$), and the texture is the ground-truth image. The result is the projection of the natural image onto the UV map. However, as can be seen in the figure, this process erroneously projects occluded vertices (the back of the car in the example), which should ideally be masked out as visual information associated with them is not available in the 2D image. We therefore mask the projection using a binary *visibility mask*, which describes what parts of the mesh are visible in UV space. The mask is obtained by rendering the mesh using a dummy texture (e.g. all white) and

¹In an inference model this would be detrimental to generalization, but our goal is mesh fitting.

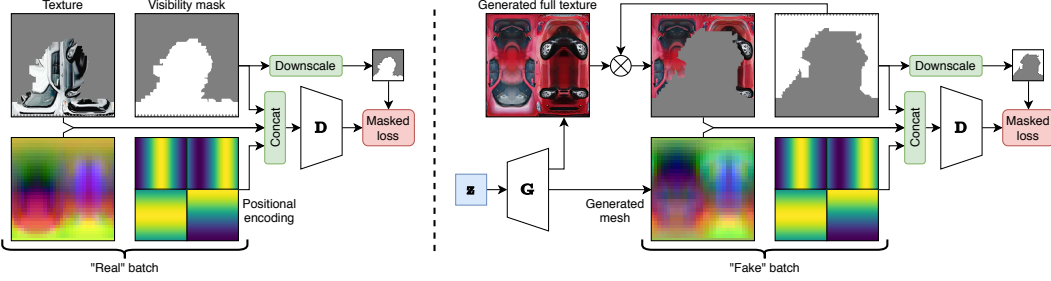


Figure 3: GAN training strategy. **Left:** discrimination of a “real” batch with *pseudo*-ground-truth textures. **Right:** discrimination of a “fake” batch after masking to reflect the “real” batch distribution.

computing its gradient with respect to the texture (we provide implementation details in the Appendix A.2). Only *texels* (pixels of the texture) that contribute to the final image (i.e. visible ones) will have non-zero gradients, therefore we obtain the visibility mask by thresholding these gradients. The final result is a pose-independent dataset of *pseudo*-ground-truth textures (because they are partially occluded). A useful consequence of this representation is that samples become semantically aligned, i.e. the positions of parts such as wheels or eyes are aligned across all images.

3.2 GAN framework

We directly use the estimated displacement maps and the *pseudo*-ground-truth textures to train a convolutional GAN, with the only obstacle that “real” textures are masked, while generated textures should ideally be complete. This can be easily dealt with by masking “fake” images before they reach **D**: as shown in Fig. 3, we multiply the batch of generated textures with a random sample of visibility masks from the training set. This strategy avoids a distribution mismatch between fake and real textures in **D**, while acting as a gradient gate such that only gradients from the visible areas will reach the generator. Being convolutional and agnostic to the visibility mask, **G** will always generate the full texture.

In terms of architecture, the generator is a convolutional model that outputs both mesh (displacement map) and texture. Mesh and texture can have different resolutions – in our experiments we use 32×32 for the mesh and up to 512×512 for the texture. To support this, the generator branches out at some point and outputs mesh and texture through two different heads (this is also done in the *mesh estimation* model). The discriminator adopts a multi-scale architecture [47] (i.e. multiple discriminators trained jointly) and a patch-based loss [19] which is masked using the visibility mask scaled to the same resolution as the last feature map. The smallest discriminator discriminates both the mesh and the texture, which is downsampled to the same resolution as the mesh (32×32). It focuses on global aspects of the texture, while discriminating the mesh and how well it fits the texture. The higher-resolution discriminators are only texture discriminators (one for experiments at 256×256 , two for experiments at 512×512 in which the intermediate one discriminates at 128×128).

D takes as input the displacement map (mesh), the masked texture, the visibility mask, as well as a *soft* positional encoding of the UV map: inspired by attention-based NLP methods that propose a similar idea [45] (unrelated to our attention method for text conditioning), we add a sinusoidal encoding to the input that gives convolutions a sense of where they are within the image. For a coordinate space $u, v \in [-1, 1]$, we add four channels $\cos(\pi u), \sin(\pi u), \cos(\pi(v/2 + 0.5)), \sin(\pi(v/2 + 0.5))$ such that the encoding smoothly wraps around the u (horizontal) axis and is discontinuous along the v (vertical) axis. Giving an absolute sense of position to the model is important as the semantics of the *texels* depend on their absolute position within the UV map, and we show this quantitatively in the ablations (sec. 4.3). Finally, the GAN framework allows us to condition the generator on a wide range of inputs: class labels, classes combined with attributes, and text. For the latter, we investigate both an attention mechanism and a method based on a simple fixed-length sentence embedding. We explain how these are implemented in sec. 4.2.

4 Experiments

4.1 Evaluation and datasets

Perceptual metrics such as the Fréchet Inception Distance (FID) [16] are widely employed for evaluating 2D GANs, as they have been shown to correlate well with human judgment [62]. Although

we focus on a different task, the FID still appears as a natural choice as it can easily be adapted to our task. Therefore, we suggest to evaluate FID scores on rendered 2D projections of generated meshes. To this end, we sample random poses (i.e. viewpoints) from the training set as we do not want the evaluation metric to be affected by our choice of poses. Moreover, this strategy allows us to evaluate mesh and texture separately: in addition to the *Full FID*, we report the *Texture FID*, where we use meshes estimated using the differentiable renderer instead of generated ones, and the *Mesh FID*, where we replace generated textures with *pseudo*-ground-truth ones. In the latter, using real poses ensures that we render the visible part of the *pseudo*-ground-truth texture, and occlusions are minimized. While we mostly rely on the *Full FID* to discuss our results, the individual ones represent a useful tool for analyzing how the model responds to variations of the architecture. Generated samples are rendered at 299×299 (the native resolution of Inception), and ground-truth images are also scaled to this resolution. In the Appendix A.2, we provide some visualizations that give more insight into the conceptual differences between these metrics.

We evaluate our method on two datasets with annotated keypoints, and use the implementation of [21] to estimate the pose from keypoints using structure-from-motion.

CUB-200-2011 [46] We use the train/test split of [21], which consists of $\approx 6k$ training images and $\approx 5.7k$ test images. Each image has an annotated class label (out of 200 classes) and 10 captions which we use for text conditioning. Using poses and labels (where applicable) from the training set, we evaluate the FID on test images, although we observe that the FID is almost identical between the two sets.

Pascal3D+ (P3D) [51] We use the *cars* subset, which is the most abundant class in this dataset. Images are part of a low-resolution set (Pascal set) and a newer, high-resolution set from ImageNet [6]. While we use the same split as [21] to train our mesh estimation model, the GAN is trained only on the ImageNet subset ($\approx 4.7k$ usable images) since we noticed that the images in the Pascal set are too small for practical purposes. We infer segmentation masks using Mask R-CNN [13] since they are not available. The test split of [21] does not contain any ImageNet images, therefore we evaluate FID scores on training images², motivated by our previous observation on CUB. Finally, to demonstrate conditional generation on this dataset, we collected new annotations for the class (11 shape categories) and color (11 attributes) of each car (details and statistics in the Appendix A.2).

4.2 Implementation details

Mesh estimation. The model (Fig. 1) is trained for 1000 epochs using Adam [25], with an initial learning rate of 10^{-4} halved every 250 epochs. We train with a batch size of 50, which requires ≈ 12 hours on a single Pascal GPU. We use DIB-R [4] for differentiable rendering due to its support for texture mapping and its relatively low overhead. To stabilize training we adopt a warm-up phase, described in the Appendix A.2. In the same section we also describe how we augment the camera model for Pascal3D+. Finally, the detailed architecture of the network can be found in the Appendix A.1.

GAN architecture. Since our method is reduced to a 2D generation task, we adopt recent ideas from the 2D convolutional GAN literature. Our generator follows a ResNet architecture where the latent code \mathbf{z} (64D, normally distributed) is injected in the input layer as well as after every convolutional layer through *conditional batch normalization*. Following [59, 3], we use spectral normalization [31] in both \mathbf{G} and \mathbf{D} , but \mathbf{D} does not employ further normalization, e.g. we tried instance normalization but found it detrimental. We adopt a hinge loss objective (patch-based and masked as described in sec. 3), and train for 600 epochs with a constant learning rate of 0.0001 for \mathbf{G} and 0.0004 for \mathbf{D} (two time-scale update rule [16]). We update \mathbf{D} twice per \mathbf{G} update, and evaluate the model on a running average of \mathbf{G} 's weights ($\beta = 0.999$) as proposed by [58, 22, 23, 3]. Detailed aspects about the architecture of our GAN can be found in the Appendix A.1. Training the 512×512 models requires ≈ 20 hours on 4 Pascal GPUs, while the 256×256 models require roughly the same time on a single GPU.

Conditional generation. In settings conditioned on class labels, we simply concatenate a learnable 64D embedding to \mathbf{z} , and use *projection discrimination* [32] in the last feature map of \mathbf{D} . In the P3D experiment with attributes (i.e. colors), we split the embedding into a 32D shape embedding and a 32D color embedding. For text conditioning, we first encode the sentence using the pretrained RNN encoder from [53], and compare (i) a simple method where we concatenate the sentence embedding to \mathbf{z} as before, (ii) an attention mechanism operating on all hidden states of the RNN. For the latter we add a single attention layer in \mathbf{G} right before the mesh/texture branching, operating at 16×16

²Given the already small size of the dataset, we decided not to split it further.

resolution. Likewise, we modify projection discrimination in \mathbf{D} to apply attention on the last feature map. Detailed schemes can be found in the Appendix A.1.

Representation. Since the UV map of a UV sphere has circular boundary conditions along the horizontal axis, convolutional layers in the discriminator use circular padding horizontally and regular zero-padding vertically. Furthermore, in both the mesh estimation model and the GAN generator, we enforce reflectional symmetry across the x axis as done in [21], which has the dual benefit of improving quality and halving the computational cost to output a mesh/texture. In this case, convolutions use reflection padding horizontally instead of circular padding. Finally, to deal with the singularities of the UV sphere, the vertex displacements of the north and south pole are respectively taken to be the average of the top and bottom rows of the displacement map.

4.3 Results

Table 1: **Left:** FID scores grouped by dataset, texture resolution, and conditioning, both in truncated and untruncated settings. Lower is better; bold = best. **Right:** Ablation study on CUB with a 512×512 texture resolution. We report truncated FID scores in the truncated setting.

Dataset	Tex. Res.	Conditioning	σ	FID (truncated σ)			FID (untruncated)			FID	Δ
				Full	Tex.	Mesh	Full	Tex.	Mesh		
CUB	512x512	None	1	41.56	45.26	18.36	56.27	50.12	25.85	33.63	0
		Class	0.25	33.63	28.68	19.49	41.33	30.60	23.28	43.71	+10.08
		Text	0.5	18.45	22.91	12.05	42.66	38.95	21.18	41.55	+7.92
P3D	512x512	Class	0.25	33.55	30.92	19.39	42.61	33.31	23.37	36.38	+2.75
		None	1	43.09	32.70	28.62	74.74	47.99	43.23	18.45	0
		Class	0.75	27.73	22.17	23.76	49.56	29.98	34.10	22.14	+3.69
	256x256	Class+Color	0.5	31.30	21.70	27.75	52.55	30.29	36.32		
	256x256	Class+Color	0.5	39.09	26.52	36.73	63.63	36.56	46.37		



Figure 4: Qualitative results on P3D (left, conditioned on class *and* color) and CUB (right, conditioned on class). Each object is rendered from 3 views, and the top row depicts the unwrapped texture.

Quantitative results. We report our main results in Table 1 (left). For CUB, we compare settings where the model is conditioned on class labels, captions (using the attention model), and no conditioning at all. For P3D, we compare unconditional generation and conditional generation on class labels (i.e. car shapes) as well as classes *plus* colors. We evaluate the FID every 20 epochs and report the model with the best *Full FID* in the table. Since there is no prior work to which we can compare under our setting, we set baselines on these two datasets. As proposed by [3], we found it useful to sample latent codes \mathbf{z} from a truncated Gaussian (only at inference time), which trades off sample diversity for quality and considerably improves FID scores. For each setting we specify the optimal truncation σ , but we also report scores in an untruncated setting as these are more directly comparable. As expected, conditional GANs result in better scores than their unconditional counterparts (with the text model being the best), but we generally observe that our approach is stable under all settings.

Ablation study. We conduct an ablation study in Table 1 (right). The results in the top section are relative to the 512×512 CUB model conditioned on classes (truncated FID). Removing the positional encoding from the discriminator leads to a significant FID degradation (+10.08), suggesting that giving convolutions a sense of absolute position in UV space is an important aspect of our approach. Likewise, updating \mathbf{D} as often as \mathbf{G} has a significant negative impact (+7.92) compared to two \mathbf{D} updates per \mathbf{G} update. Using instance normalization in \mathbf{D} also leads to a slight degradation (+2.75),

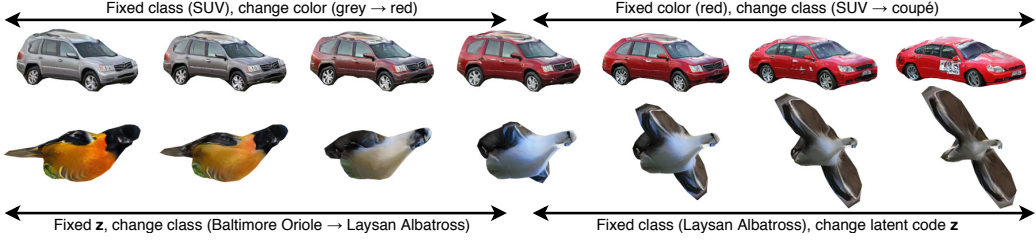


Figure 5: Interpolation over conditioning inputs, which highlights that our model learns a structured latent space where factors of variation of both shape and texture are relatively disentangled.



Figure 6: **Left:** generated meshes rendered from random viewpoints on P3D and CUB, both conditioned on a random set of classes. **Right:** generation from text on CUB, which allows for fine control over both texture and mesh. We modify captions incrementally, where changes are highlighted in bold.

but beyond that we observe that, while training appears to converge faster initially, it rapidly becomes unstable. In the bottom section of the table, we compare the text attention model (baseline) to a model where a fixed-length sentence vector is simply concatenated to \mathbf{z} (as in the other conditional models). The results show that the model effectively exploits the attention mechanism with the added benefit of being more interpretable (we show a few visualizations in the Appendix A.3).

Qualitative results. Fig. 4 shows a few generated meshes rendered from multiple viewpoints, as well as the corresponding textures. While results on CUB are generally of high visual quality, we observe that the back of the cars in P3D present some artifacts. After further investigation, we found that the dataset is very imbalanced, with only 10–20% of the images depicting the back of the car and the majority depicting the front. Therefore, this issue could in principle be mitigated with more training data. In Fig. 5 we show that the latent space of our models is structured. We interpolate over different factors of variation using spherical interpolation and observe that they are relatively disentangled, enabling isolated control over shape, color, and style in addition to the pose disentanglement guaranteed by the 3D representation itself. Fig. 6 shows results rendered from random viewpoints (the scenario on which we evaluate FID scores) as well as generation conditioned on text, which enables precise control over both shape and appearance. Finally, in the Appendix A.3 we show a wider range of qualitative results.

5 Conclusion

We propose a GAN-based framework for generating 3D meshes. Our approach can generate triangle meshes and corresponding texture maps at high-resolution (512×512 and possibly more), requiring only 2D supervision from single-view natural images. We evaluate our method on Pascal3D+ Cars and CUB Birds, and showcase it under a wide range of conditional settings to demonstrate its high level of adaptation. Nonetheless, we have only scratched the surface of what can be done with this framework. Our approach can be enriched by employing different forms of supervision (e.g. semi-supervision by combining 3D supervision from synthetic datasets with 2D supervision from natural images) as well as incorporating more conditional information that would allow the model to disentangle further aspects of variation (e.g. lighting). In the future, we would also like to experiment with more data.

Acknowledgments

This work was partly supported by the Swiss National Science Foundation (SNF), grant #176004, and Research Foundation Flanders (FWO), grant G078618N. Additionally, Graham Spinks and Marie-Francine Moens are partly funded by an ERC Advanced Grant, #788506.

References

- [1] P. Achlioptas, O. Diamanti, I. Mitliagkas, and L. Guibas. Learning representations and generative models for 3d point clouds. In *International Conference on Machine Learning*, pages 40–49, 2018.
- [2] E. Balashova, V. Singh, J. Wang, B. Teixeira, T. Chen, and T. Funkhouser. Structure-aware shape synthesis. In *2018 International Conference on 3D Vision (3DV)*, pages 140–149. IEEE, 2018.
- [3] A. Brock, J. Donahue, and K. Simonyan. Large scale GAN training for high fidelity natural image synthesis. In *International Conference on Learning Representations (ICLR)*, 2019.
- [4] W. Chen, H. Ling, J. Gao, E. Smith, J. Lehtinen, A. Jacobson, and S. Fidler. Learning to predict 3d objects with an interpolation-based differentiable renderer. In *Neural Information Processing Systems*, pages 9605–9616, 2019.
- [5] C. B. Choy, D. Xu, J. Gwak, K. Chen, and S. Savarese. 3d-r2n2: A unified approach for single and multi-view 3d object reconstruction. In *European conference on computer vision*, pages 628–644. Springer, 2016.
- [6] J. Deng, W. Dong, R. Socher, L.-J. Li, K. Li, and L. Fei-Fei. Imagenet: A large-scale hierarchical image database. In *IEEE Conference on Computer Vision and Pattern Recognition (CVPR)*, pages 248–255. IEEE, 2009.
- [7] H. Fan, H. Su, and L. J. Guibas. A point set generation network for 3d object reconstruction from a single image. In *Proceedings of the IEEE Conference on Computer Vision and Pattern Recognition*, pages 605–613, 2017.
- [8] M. Gadelha, R. Wang, and S. Maji. Multiresolution tree networks for 3d point cloud processing. In *Proceedings of the European Conference on Computer Vision (ECCV)*, pages 103–118, 2018.
- [9] R. Girdhar, D. F. Fouhey, M. Rodriguez, and A. Gupta. Learning a predictable and generative vector representation for objects. In *European Conference on Computer Vision*, pages 484–499. Springer, 2016.
- [10] I. Goodfellow, J. Pouget-Abadie, M. Mirza, B. Xu, D. Warde-Farley, S. Ozair, A. Courville, and Y. Bengio. Generative adversarial nets. In *Neural Information Processing Systems*, pages 2672–2680, 2014.
- [11] J. Gwak, C. B. Choy, M. Chandraker, A. Garg, and S. Savarese. Weakly supervised 3d reconstruction with adversarial constraint. In *2017 International Conference on 3D Vision (3DV)*, pages 263–272. IEEE, 2017.
- [12] C. Häne, S. Tulsiani, and J. Malik. Hierarchical surface prediction for 3d object reconstruction. In *2017 International Conference on 3D Vision (3DV)*, pages 412–420. IEEE, 2017.
- [13] K. He, G. Gkioxari, P. Dollár, and R. Girshick. Mask R-CNN. In *IEEE International Conference on Computer Vision (ICCV)*, pages 2961–2969, 2017.
- [14] P. Henderson, V. Tsiminaki, and C. H. Lampert. Leveraging 2d data to learn textured 3d mesh generation. In *Proceedings of the IEEE Conference on Computer Vision and Pattern Recognition*, 2020.
- [15] P. Henzler, N. J. Mitra, and T. Ritschel. Escaping plato’s cave: 3d shape from adversarial rendering. In *Proceedings of the IEEE International Conference on Computer Vision*, pages 9984–9993, 2019.
- [16] M. Heusel, H. Ramsauer, T. Unterthiner, B. Nessler, and S. Hochreiter. GANs trained by a two time-scale update rule converge to a local Nash equilibrium. In *Neural Information Processing Systems*, pages 6626–6637, 2017.
- [17] S. Hong, D. Yang, J. Choi, and H. Lee. Inferring semantic layout for hierarchical text-to-image synthesis. In *IEEE Conference on Computer Vision and Pattern Recognition (CVPR)*, pages 7986–7994, 2018.
- [18] E. Insafutdinov and A. Dosovitskiy. Unsupervised learning of shape and pose with differentiable point clouds. In *Advances in Neural Information Processing Systems*, pages 2802–2812, 2018.

- [19] P. Isola, J.-Y. Zhu, T. Zhou, and A. A. Efros. Image-to-image translation with conditional adversarial networks. In *IEEE Conference on Computer Vision and Pattern Recognition (CVPR)*, pages 1125–1134, 2017.
- [20] J. Johnson, A. Gupta, and L. Fei-Fei. Image generation from scene graphs. In *IEEE Conference on Computer Vision and Pattern Recognition (CVPR)*, pages 1219–1228, 2018.
- [21] A. Kanazawa, S. Tulsiani, A. A. Efros, and J. Malik. Learning category-specific mesh reconstruction from image collections. In *European Conference on Computer Vision (ECCV)*, 2018.
- [22] T. Karras, T. Aila, S. Laine, and J. Lehtinen. Progressive growing of GANs for improved quality, stability, and variation. In *International Conference on Learning Representations (ICLR)*, 2018.
- [23] T. Karras, S. Laine, and T. Aila. A style-based generator architecture for generative adversarial networks. In *IEEE Conference on Computer Vision and Pattern Recognition (CVPR)*, pages 4401–4410, 2019.
- [24] H. Kato, Y. Ushiku, and T. Harada. Neural 3D mesh renderer. In *IEEE Conference on Computer Vision and Pattern Recognition (CVPR)*, pages 3907–3916, 2018.
- [25] D. P. Kingma and J. Ba. Adam: A method for stochastic optimization. In *International Conference on Learning Representations (ICLR)*, 2014.
- [26] D. P. Kingma and M. Welling. Auto-encoding variational Bayes. In *International Conference on Learning Representations (ICLR)*, 2014.
- [27] B. Li, X. Qi, T. Lukasiewicz, and P. H. S. Torr. Controllable text-to-image generation. In *Neural Information Processing Systems*, December 2019.
- [28] S. Liu, T. Li, W. Chen, and H. Li. Soft rasterizer: A differentiable renderer for image-based 3d reasoning. In *IEEE International Conference on Computer Vision (ICCV)*, pages 7708–7717, 2019.
- [29] F. Locatello, S. Bauer, M. Lucic, S. Gelly, B. Schölkopf, and O. Bachem. Challenging common assumptions in the unsupervised learning of disentangled representations. In *International Conference on Machine Learning (ICML)*, 2019.
- [30] M. M. Loper and M. J. Black. Opendr: An approximate differentiable renderer. In *European Conference on Computer Vision (ECCV)*, pages 154–169. Springer, 2014.
- [31] T. Miyato, T. Kataoka, M. Koyama, and Y. Yoshida. Spectral normalization for generative adversarial networks. In *International Conference on Learning Representations (ICLR)*, 2018.
- [32] T. Miyato and M. Koyama. cGANs with projection discriminator. In *International Conference on Learning Representations (ICLR)*, 2018.
- [33] S. Mo, M. Cho, and J. Shin. Instance-aware image-to-image translation. In *International Conference on Learning Representations (ICLR)*, 2019.
- [34] A. Odena, V. Dumoulin, and C. Olah. Deconvolution and checkerboard artifacts. *Distill*, 2016.
- [35] J. J. Park, P. Florence, J. Straub, R. Newcombe, and S. Lovegrove. DeepSDF: Learning continuous signed distance functions for shape representation. In *IEEE Conference on Computer Vision and Pattern Recognition (CVPR)*, pages 165–174, 2019.
- [36] T. Park, M.-Y. Liu, T.-C. Wang, and J.-Y. Zhu. Semantic image synthesis with spatially-adaptive normalization. In *IEEE Conference on Computer Vision and Pattern Recognition (CVPR)*, pages 2337–2346, 2019.
- [37] D. J. Rezende, S. A. Eslami, S. Mohamed, P. Battaglia, M. Jaderberg, and N. Heess. Unsupervised learning of 3d structure from images. In *Advances in Neural Information Processing Systems*, pages 4996–5004, 2016.
- [38] K. K. Singh, U. Ojha, and Y. J. Lee. FineGAN: Unsupervised hierarchical disentanglement for fine-grained object generation and discovery. In *IEEE Conference on Computer Vision and Pattern Recognition (CVPR)*, 2019.
- [39] E. J. Smith and D. Meger. Improved adversarial systems for 3d object generation and reconstruction. In *Conference on Robot Learning*, pages 87–96, 2017.
- [40] O. Sorkine, D. Cohen-Or, Y. Lipman, M. Alexa, C. Rössl, and H.-P. Seidel. Laplacian surface editing. In *Eurographics/ACM SIGGRAPH Symposium on Geometry Processing*, pages 175–184, 2004.

- [41] W. Sun and T. Wu. Image synthesis from reconfigurable layout and style. In *IEEE International Conference on Computer Vision (ICCV)*, pages 10531–10540, 2019.
- [42] M. Tatarchenko, A. Dosovitskiy, and T. Brox. Octree generating networks: Efficient convolutional architectures for high-resolution 3d outputs. In *Proceedings of the IEEE International Conference on Computer Vision*, pages 2088–2096, 2017.
- [43] S. Tulsiani, A. A. Efros, and J. Malik. Multi-view consistency as supervisory signal for learning shape and pose prediction. In *Proceedings of the IEEE Conference on Computer Vision and Pattern Recognition*, pages 2897–2905, 2018.
- [44] S. Tulsiani, T. Zhou, A. A. Efros, and J. Malik. Multi-view supervision for single-view reconstruction via differentiable ray consistency. In *Proceedings of the IEEE Conference on Computer Vision and Pattern Recognition*, pages 2626–2634, 2017.
- [45] A. Vaswani, N. Shazeer, N. Parmar, J. Uszkoreit, L. Jones, A. N. Gomez, Ł. Kaiser, and I. Polosukhin. Attention is all you need. In *Neural Information Processing Systems*, pages 5998–6008, 2017.
- [46] C. Wah, S. Branson, P. Welinder, P. Perona, and S. Belongie. The Caltech-UCSD Birds-200-2011 dataset. Technical Report CNS-TR-2011-001, California Institute of Technology, 2011.
- [47] T.-C. Wang, M.-Y. Liu, J.-Y. Zhu, A. Tao, J. Kautz, and B. Catanzaro. High-resolution image synthesis and semantic manipulation with conditional GANs. In *IEEE Conference on Computer Vision and Pattern Recognition (CVPR)*, pages 8798–8807, 2018.
- [48] O. Wiles and A. Zisserman. Silnet : Single- and multi-view reconstruction by learning from silhouettes. In G. B. Tae-Kyun Kim, Stefanos Zafeiriou and K. Mikolajczyk, editors, *Proceedings of the British Machine Vision Conference (BMVC)*, pages 99.1–99.13. BMVA Press, September 2017.
- [49] J. Wu, Y. Wang, T. Xue, X. Sun, B. Freeman, and J. Tenenbaum. Marrnet: 3d shape reconstruction via 2.5d sketches. In *Neural Information Processing Systems*, pages 540–550, 2017.
- [50] J. Wu, C. Zhang, T. Xue, B. Freeman, and J. Tenenbaum. Learning a probabilistic latent space of object shapes via 3d generative-adversarial modeling. In *Advances in Neural Information Processing Systems*, pages 82–90, 2016.
- [51] Y. Xiang, R. Mottaghi, and S. Savarese. Beyond PASCAL: A benchmark for 3D object detection in the wild. In *IEEE Winter Conference on Applications of Computer Vision (WACV)*, 2014.
- [52] J. Xie, Z. Zheng, R. Gao, W. Wang, S.-C. Zhu, and Y. Nian Wu. Learning descriptor networks for 3d shape synthesis and analysis. In *Proceedings of the IEEE conference on computer vision and pattern recognition*, pages 8629–8638, 2018.
- [53] T. Xu, P. Zhang, Q. Huang, H. Zhang, Z. Gan, X. Huang, and X. He. AttnGAN: Fine-grained text to image generation with attentional generative adversarial networks. In *IEEE Conference on Computer Vision and Pattern Recognition (CVPR)*, pages 1316–1324, 2018.
- [54] X. Yan, J. Yang, E. Yumer, Y. Guo, and H. Lee. Perspective transformer nets: Learning single-view 3d object reconstruction without 3d supervision. In *Advances in Neural Information Processing Systems*, pages 1696–1704, 2016.
- [55] B. Yang, H. Wen, S. Wang, R. Clark, A. Markham, and N. Trigoni. 3d object reconstruction from a single depth view with adversarial learning. In *Proceedings of the IEEE International Conference on Computer Vision Workshops*, pages 679–688, 2017.
- [56] G. Yang, Y. Cui, S. Belongie, and B. Hariharan. Learning single-view 3d reconstruction with limited pose supervision. In *Proceedings of the European Conference on Computer Vision (ECCV)*, pages 86–101, 2018.
- [57] J. Yang, A. Kannan, D. Batra, and D. Parikh. LR-GAN: layered recursive generative adversarial networks for image generation. In *International Conference on Learning Representations (ICLR)*, 2017.
- [58] Y. Yazici, C.-S. Foo, S. Winkler, K.-H. Yap, G. Piliouras, and V. Chandrasekhar. The unusual effectiveness of averaging in GAN training. In *International Conference on Learning Representations (ICLR)*, 2019.
- [59] H. Zhang, I. Goodfellow, D. Metaxas, and A. Odena. Self-attention generative adversarial networks. In *International Conference on Machine Learning (ICML)*, 2019.

- [60] H. Zhang, T. Xu, H. Li, S. Zhang, X. Wang, X. Huang, and D. N. Metaxas. StackGAN: Text to photo-realistic image synthesis with stacked generative adversarial networks. In *IEEE International Conference on Computer Vision (ICCV)*, pages 5907–5915, 2017.
- [61] H. Zhang, T. Xu, H. Li, S. Zhang, X. Wang, X. Huang, and D. N. Metaxas. StackGAN++: Realistic image synthesis with stacked generative adversarial networks. *IEEE Transactions on Pattern Analysis and Machine Intelligence (TPAMI)*, 41(8):1947–1962, 2018.
- [62] R. Zhang, P. Isola, A. A. Efros, E. Shechtman, and O. Wang. The unreasonable effectiveness of deep features as a perceptual metric. In *IEEE Conference on Computer Vision and Pattern Recognition (CVPR)*, pages 586–595, 2018.
- [63] B. Zhao, L. Meng, W. Yin, and L. Sigal. Image generation from layout. In *IEEE Conference on Computer Vision and Pattern Recognition (CVPR)*, pages 8584–8593, 2019.
- [64] J.-Y. Zhu, T. Park, P. Isola, and A. A. Efros. Unpaired image-to-image translation using cycle-consistent adversarial networks. In *IEEE International Conference on Computer Vision (ICCV)*, pages 2223–2232, 2017.
- [65] J.-Y. Zhu, Z. Zhang, C. Zhang, J. Wu, A. Torralba, J. Tenenbaum, and B. Freeman. Visual object networks: Image generation with disentangled 3d representations. In *Neural Information Processing Systems*, pages 118–129, 2018.
- [66] R. Zhu, H. Kiani Galoogahi, C. Wang, and S. Lucey. Rethinking reprojection: Closing the loop for pose-aware shape reconstruction from a single image. In *Proceedings of the IEEE International Conference on Computer Vision*, pages 57–65, 2017.

A Supplementary material

A.1 Detailed architecture

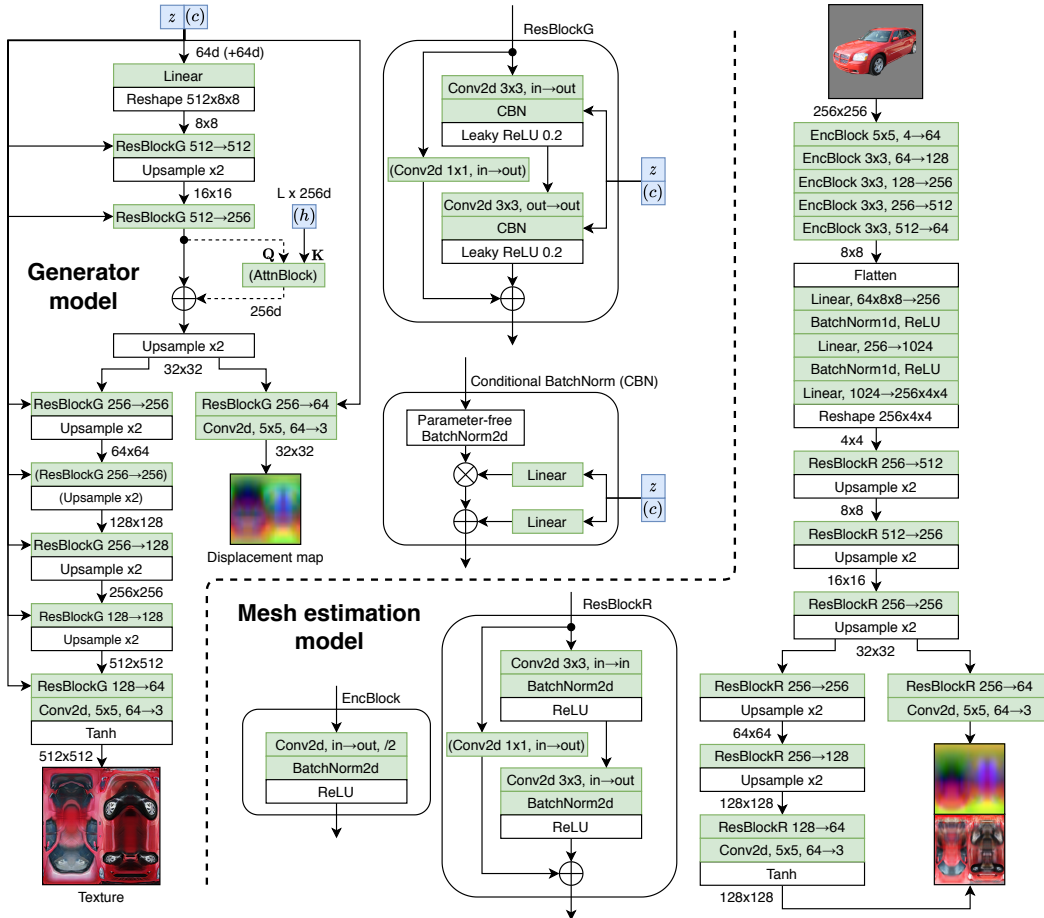


Figure 7: Generator architecture (left) and mesh estimation model (right). Green blocks comprise learnable parameters, whereas white ones are parameter-free. Dashed lines and blocks in parentheses represent optional connections which depend on the specific setting. We indicate the feature map resolution in a given position next to arrows (e.g. 128×128). $512 \rightarrow 256$ denotes “ 512 input channels, 256 output channels”. “/2” in convolutional layers denotes “stride 2”; it is one if not indicated.

Generator. Fig. 7 (left) shows the detailed architecture of the generator of our GAN. As mentioned in sec. 4.2, the random vector z is fed to every conditional batch normalization (CBN) layer as well as the input layer, which matches the strategy adopted by many state-of-the-art GANs for 2D image generation [32, 59, 3]. A CBN layer consists of a parameter-free batch normalization (i.e. without a learned affine transformation) followed by a gain γ and bias β conditioned upon z via a learned linear layer. In settings conditioned on class labels, we concatenate a learned embedding c to z , which is shared among all layers. The network follows a ResNet architecture where feature maps are progressively upsampled using nearest-neighbor interpolation after each residual block ResBlockG. This block consists of two convolutional layers wrapped by a skip-connection. If the number of input channels differs from the number of output channels, the skip-connection is learned. To accommodate for the varying output resolutions for mesh and texture, the generator branches out at 32×32 resolution. While the figure shows the architecture for 512×512 textures, to generate textures at 256×256 we simply remove one $256 \rightarrow 256$ ResBlockG block. For presentation purposes, we report square resolutions (e.g. 512×512), but in practice we only need to generate half of the feature map (e.g. 256×512) since we enforce symmetry across the x axis as mentioned in sec. 4.2. The output textures and displacement maps are then simply padded with their reflection. On the other hand, the discriminator always observes full textures as *pseudo*-ground-truth textures are asymmetric.

Attention mechanism. If the model is conditioned on text using an attention mechanism, we add an attention block right before the texture/mesh branch, so that the module influences both mesh and texture. We adopt a dot-product formulation similar to [53], in which the attention weights are computed as $\text{softmax}(\mathbf{Q}\mathbf{K}^T)$. The queries \mathbf{Q} correspond to the flattened convolutional feature map from the generator, and the keys \mathbf{K} are obtained by passing each RNN hidden state \mathbf{h}_l ($l \in \{1..L\}$, where L is the sentence length) through a learned linear layer. The RNN is the pretrained bidirectional LSTM encoder from [53], and hidden states are 256-dimensional.

Mesh estimation model. Fig. 7 (right) shows the detailed architecture of the mesh estimation model that we use for differentiable rendering (the first step of our algorithm as described in Fig. 1). The natural image is concatenated to the segmentation mask (3+1 channels) and fed to a convolutional encoder. The representation is then flattened to a dense representation and passed through a series of linear layers. Finally, it is passed through a ResNet decoder whose architecture resembles that of the GAN generator. Since we are not interested in producing high-quality textures in this step as they are discarded, the texture resolution in this model is only 128×128 , which results in faster training.

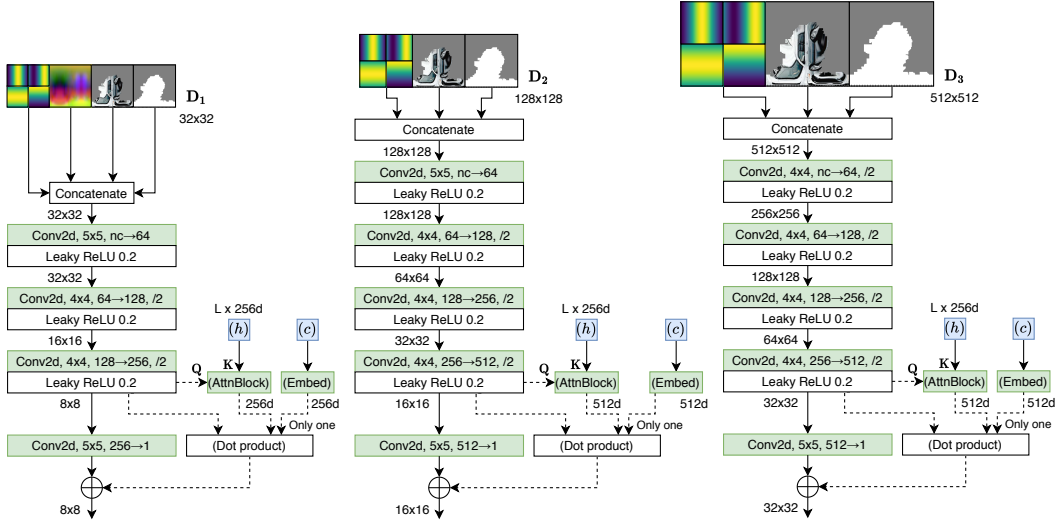


Figure 8: Multi-scale discriminator architecture for our biggest model (512×512 texture resolution). Only D_1 discriminates the mesh, while D_2 and D_3 are texture discriminators. Dashed lines describe the optional connections for *projection discrimination* [32] in conditional settings, where feature maps are combined *either* with a learned embedding (for settings conditioned on classes or attributes) or with the values of an attention block (for settings conditioned on text), not both.

Discriminator. The architecture of our multi-scale discriminator is depicted in Fig. 8. In the 512×512 setting, textures are discriminated at three scales: 32×32 (D_1), 128×128 (D_2), and 512×512 (D_3). The smallest discriminator D_1 is also a mesh discriminator. Following the general strategy of patch-based discriminators [19], our discriminators are relatively simple as they only consist of a series of spectrally-normalized convolutional layers. GANs have been shown to produce checkerboard artifacts [34] depending on the choice of kernel sizes and strides in the discriminator. While humans do not perceive these to be particularly severe in images, checkerboard artifacts in the *displacement map* must be avoided as they might lead to noticeable mesh distortions. The generator already uses upsampling instead of transposed convolutions (which mitigates this issue), but we also carefully design the discriminator such that the kernel size of convolutions is divisible by the stride, ensuring that the gradient norms are uniform across pixels (see [34] for further details). To this end, we use 5×5 convolutions in layers with stride 1, and 4×4 convolutions in layers with stride 2. D_1 consists of 4 layers and has a relatively small receptive field. We explored a varying number of layers and different strides, but they always led to worse results. D_2 and D_3 consist of 5 layers and are identical except for the stride of the first layer, which is 1 for D_2 and 2 for D_3 . In the experiments with a texture resolution of 256×256 , we only use D_1 and D_2 , where the latter directly discriminates at 256×256 . Finally, to incorporate conditional information, we use *projection discrimination* [32], in which we compute a pixel-wise dot product between the last feature map and a learned class embedding, and add it to the output. If the model is conditioned on text, we replace the class embedding with the output of an attention block. Each discriminator learns its own set of weights for the embeddings or the attention block.

Model complexity. Table 2 summarizes the complexity of our models in different settings, expressed as the number of learnable parameters. Since the semantic alignment of our pose-independent representation facilitates the modeling task, our approach can successfully work with relatively small models ($\approx 10M$ generator parameters). We also found it beneficial to adopt simple discriminators compared to the generator (which is more powerful).

Table 2: Number of learnable parameters for different variants of our model.

Model	Resolution	G	D ₁	D ₂	D ₃	D Total	RNN
Unconditional	512x512	11.58M	0.68M	2.77M	2.77M	6.22M	-
	256x256	10.33M	-	-	3.45M	-	
CUB conditional	512x512	13.06M	0.73M	2.88M	2.88M	6.49M	-
	256x256	11.75M	-	-	3.61M	-	
CUB text	512x512	11.64M	0.75M	2.91M	2.91M	6.57M	2.08M
P3D conditional	512x512	13.05M	0.69M	2.79M	2.79M	6.27M	-
	256x256	11.74M	-	-	3.48M	-	

A.2 Additional implementation details

Mesh estimation. Since our *convolutional mesh* representation already encourages meshes to be smooth, our reconstruction model requires less regularization than similar frameworks based on fully-connected networks. We only found it beneficial to regularize the model with a smoothness loss $\mathcal{L}_{\text{flat}}$ [24] at a very low strength $\alpha = 0.00005$, and no Laplacian regularization [40] (unlike [24, 21, 4] which all use this form of regularization). $\mathcal{L}_{\text{flat}}$ encourages the normals of neighboring faces to have similar directions, and is defined as follows:

$$\mathcal{L}_{\text{flat}} = \alpha \frac{1}{|E|} \sum_{i,j \in E} (1 - \cos \theta_{ij})^2$$

where E is the set of all edges and $\cos \theta_{ij}$ is the cosine similarity between the normals of the faces i and j . In practice this is implemented by computing the dot product between the two normals.

We additionally observe that the initialization strategy of this model as well as early training iterations have a significant impact on the final result. Bad configurations such as self-intersecting meshes or vertices outside the camera frustum can cause the model to get stuck in bad local minima from which it cannot easily recover. This is especially the case for typical Gaussian initialization schemes in neural networks, which cause the mesh to start in an already self-intersected state for a spherical mesh template with radius 1 (our case). To ensure convergence and generate smooth meshes without self-intersections, we found it helpful to (i) zero-initialize the final layer of the mesh branch, which ensures that the first iteration starts with a smooth sphere, and (ii) adopt a warm-up phase where $\mathcal{L}_{\text{flat}}$ starts at a moderate strength $\alpha = 0.0005$ and linearly decays for 100 iterations, settling at the low-strength value mentioned above. In the GAN generator we also zero-initialize the final layer of the mesh head, but $\mathcal{L}_{\text{flat}}$ only uses a fixed $\alpha = 0.0001$ and no warm-up.

In sec. 3, we mention that our camera projection model is a weak-perspective model. This model is a good approximation for photographs shot with high levels of zoom or that depict small objects, which is the case for birds (CUB dataset). However, we observed that the weak-perspective assumption is not a good fit for Pascal3D+, since most images are shot from a close range and present a significant degree of perspective distortion due to cars having elongated shapes. Therefore, for Pascal3D+ we augment the camera model with a learnable perspective correction term z_0 , without however advancing to a full perspective model as we do not have enough information. z_0 is a scalar that describes the distance from the camera to the center of the object, and assumes that the object is centered. The x, y coordinates of each vertex in camera space are then multiplied with a factor $(z_0 + z/2)/(z_0 - z/2)$, where z is the depth of the vertex. Note that, as z_0 approaches infinity, the factor approaches 1 and the camera model reverts back to a weak-perspective model. This term is learned for every image in the dataset and is parameterized as $z_0 = 1 + e^w$ (w is a learnable parameter), which ensures (i) positivity, and (ii) that the transformed vertices lie inside the camera frame. While this aspect is not central to our approach, we found it helpful as it can slightly improve qualitative results even with approximate estimates.

Construction of the pose-independent representation. In sec. 3 we mention that we use the gradient from the differentiable renderer to produce the UV visibility mask which is used for masking projected textures. In practice, deep learning frameworks do not compute full Jacobians but only gradients of scalars (i.e. Jacobian-vector multiplication). However, the Jacobian of the rendering

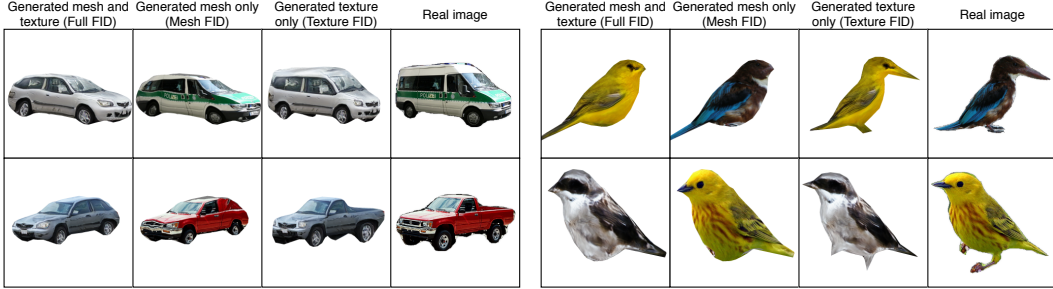


Figure 9: Examples of images on which we compute FID scores. Images are rendered from the viewpoint corresponding to *Real image* (a randomly-selected image from the training set). In the *Mesh FID* scenario, we render the generated mesh using the *pseudo*-ground-truth texture from the real image. In the *Texture FID*, the “real” mesh is textured using the generated texture. In the *Full FID* and *Mesh FID* of the top-left van we can observe that the silhouette of the mesh looks fine but straight lines and stripes present a “wobbling” effect caused by the underlying mesh, while in the *Texture FID* (which does not use generated meshes) the lines appear more straight.

operation w.r.t. the texture has a structure such that it is zero for all texels that are not visible in the rendered image (i.e. are occluded) and non-zero elsewhere³. Based on this observation, it suffices to compute the average or sum of rendered pixels to reduce the image to a scalar which can then be differentiated with respect to a dummy texture. The same result can also be achieved by computing a Jacobian-vector multiplication with a vector of ones, which is what we do in our implementation.

FID evaluation. To give more context to sec. 4.1, where we introduce our evaluation methodology, in Fig. 9 we show some actual examples of rendered images on which we compute FID scores. The *Full FID* (our main metric) is computed on generated meshes coupled with generated textures, and evaluates the generation quality as a whole. However, it is also interesting to propose variations of this metric that can evaluate mesh and texture quality separately. Therefore, in the *Mesh FID* we use the *pseudo*-ground-truth texture from the image corresponding to the random viewpoint we choose for rendering, which makes the evaluation independent of generated textures. Likewise, in the *Texture FID* we use meshes estimated using the differentiable renderer instead of the ones generated by our GAN. In all experiments, we generate as many images as there are in the set we compare to, since the FID is sensitive to the number of generated images. Finally, to evaluate text conditioning on CUB, we sample a random caption (out of 10 captions) for each image we generate.

Pascal3D+ annotations. To demonstrate conditional generation on P3D, we collected shape and color annotations for the ImageNet subset of this dataset (i.e. the one we use to train our GAN). Although ImageNet images are already identified by their *synsets*, we found these to be unreliable and opted instead for collecting our own annotations. The set of labels and corresponding frequencies are summarized in Table 3. For consistency, all labels were collected by one annotator. Some categories (e.g. *F1*, *convertible*, and *oldtimer*) comprise a very low number of samples, which leads to unsatisfactory results on these classes in conditional settings. Nonetheless, this issue can be mitigated by collecting more data. Finally, although the ImageNet subset consists of $\approx 5.5k$ images, only 4.7k are usable as some are filtered out by the structure-from-motion routine of [21] due to unreliable pose estimates.

Table 3: Relevant statistics for the P3D annotations we collected.

Class	Sedan	Hatchback	SUV	Station wagon	Van	Pickup	Coupé	City	F1	Convertible	Oldtimer	Total
# images	1137	851	814	691	674	649	295	193	119	39	13	5475
Color	Gray	Black	Red	White	Blue	Green	Yellow	Orange	Brown	Purple	Pink	Total
# images	1534	863	833	832	697	252	231	126	52	30	25	5475

A.3 Additional results

Attention mechanism visualization. Similar to other attention-based GANs conditioned on text [53], our attention mechanism can be easily visualized. Interestingly, since the attention is applied to our pose-independent representation in UV space and not on flat 2D images, our attention maps can be visualized both in UV space and on 2D renderings, as we show in Fig. 10. Furthermore, our process is more interpretable and semantically meaningful. For instance, prompts that refer to a

³This property holds for DIB-R [4] but may not hold for all differentiable renderers.



Figure 10: Visualization of the attention mechanism on our CUB model conditioned on text. The attention maps can be visualized in UV space (first row) as well as on the rendered mesh (second row). Compared to attention applied to 2D images, our mesh-attention formulation is more interpretable and does not depend on the pose of the object.



Figure 11: Generation on P3D with one varying factor at a time (color and shape) and a fixed random vector \mathbf{z} . As can be seen, representations are relatively disentangled. In the bottom row, the class *coupé* is often associated with race cars, which causes stickers to appear on the body.

specific part of the object (e.g. “yellow crown”, “red cheeks”) activate the same area within the UV map. Most importantly, these correspondences are learned in an unsupervised fashion and are aligned among different images owing to our pose-independent representation.

Disentanglement. Compared to a generative model for 2D images, a 3D generative model naturally disentangles pose and appearance. Furthermore, the use of *triangle meshes* with UV-mapped textures ensures that shape is disentangled from color, essentially allowing for texture transfer between meshes (we use this property for our *Texture FID* and *Mesh FID* evaluation, as shown in Fig. 9). Another interesting observation is that conditional models enable further disentanglement of aspects of variation. For instance, on P3D we can control shape and color separately as shown in Fig. 11, and the latent space is structured enough to allow for interpolation of these aspects (Fig. 5). In this setting, the random vector \mathbf{z} can be used to control the style of the object.

Additional qualitative results. In Fig. 12, we show additional qualitative results grouped by type of conditioning. Our approach successfully generates meshes in both conditional and unconditional settings. In the figure, we additionally show untextured (i.e. wireframe) meshes, which highlights the smoothness of our convolutional mesh representation.

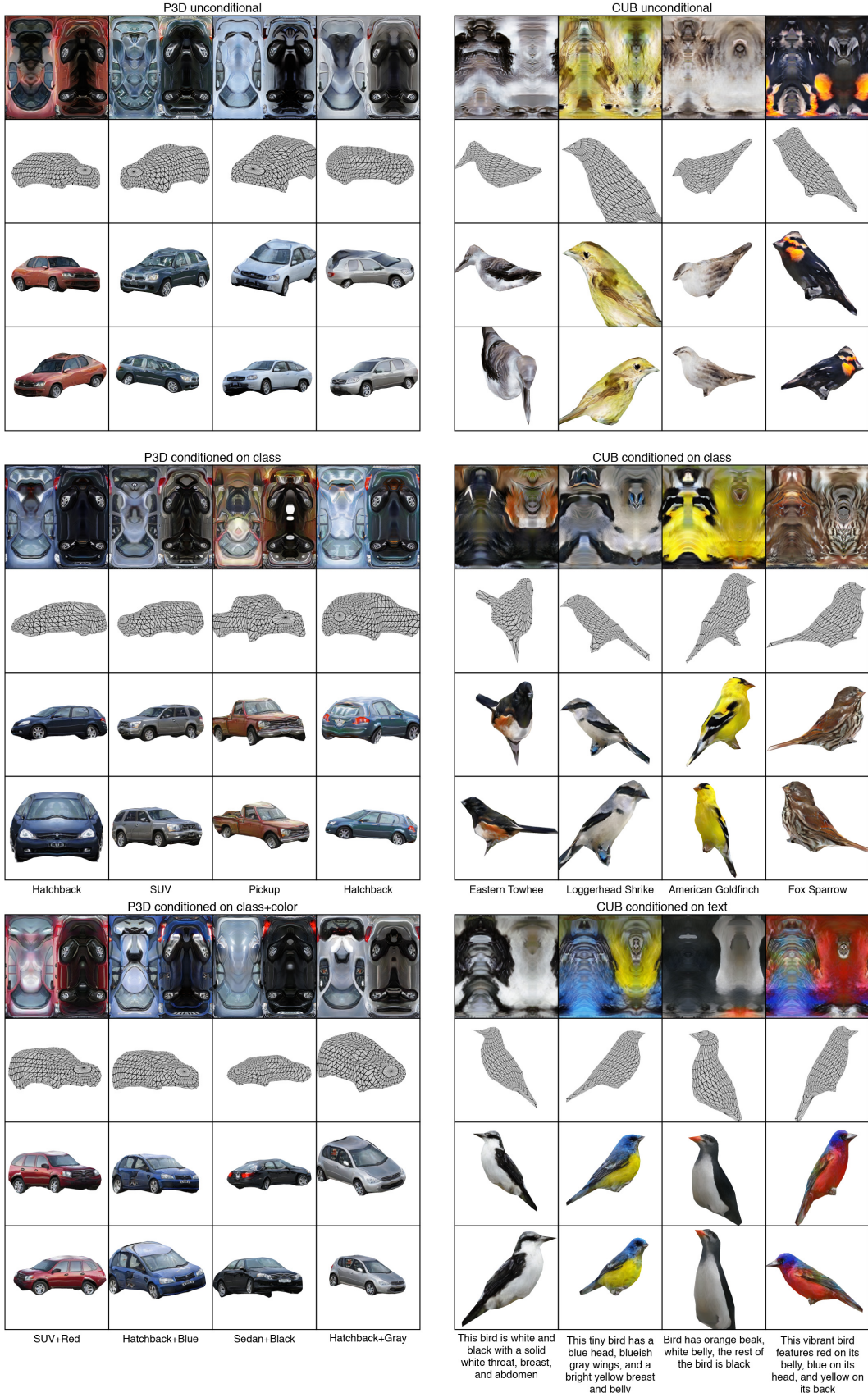


Figure 12: Qualitative results for all settings, on both P3D (left) and CUB (right). First row = texture; second row = wireframe mesh; third and fourth rows = textured object from two random views.